Journal of Controlled Release 307 (2019) 200–210

Contents lists available at ScienceDirect

Journal of Controlled Release

journal homepage: www.elsevier.com/locate/jconrel

Characterization of skin blebs from intradermal jet injection: Ex-vivo studies

Jonathan A. Simmons[a,c], Justin Davis[a], James Thomas[a], Juan Lopez[a], Andrew Le Blanc[a], Haley Allison[a], Haley Slook[a], Paul Lewis[a], Joshua Holtz[a], Paul Fisher[b], Kate E. Broderick[b], Jeremy O. Marston[a,*]

[a] Department of Chemical Engineering, Texas Tech University, Lubbock, TX 79409, United States of America
[b] Inovio Pharmaceuticals, 10480 Wateridge Circle, San Diego, CA 92121, United States of America
[c] Department of Mechanical Engineering, Texas Tech University, Lubbock, TX 79409, United States of America

ARTICLE INFO

Keywords:
Skin bleb
Needle-free injection
Liquid jet

ABSTRACT

This paper presents results from an ex-vivo study of intradermal jet injections, which is an attractive method to achieve both needle-free and fractional dose delivery of vaccines. Due to the fact that fluid properties of many novel therapeutics and vaccines can vary significantly, a key parameter for our study is the fluid viscosity, whilst the main focus is on determining the best correlation between the delivered volume and geometrical dimensions of the fluid deposit. For this we use a combination of top-view (skin wheal), underside (below the dermis), and cross-section (true skin bleb) perspectives and find that the top-view alone, as done in clinical practice, is insufficient to estimate the volume deposited in the dermis. Overall, the best correlation is found between the injection volume and cross-sectional diameter, however there is significant variation amongst the different fluids. For mean injection volumes of 60 μL the mean bleb diameter is $\approx$8 mm, with mean aspect ratio $\bar{h}/d = 0.38$, indicating the blebs are mostly oblate. However, the shape varies with viscosity and the higher viscosity does not spread laterally to the same degree as lower viscosity fluids. In addition, our high-speed video observations of the injection process, reveal some interesting dynamics of the jet injection method, and we modeled the bleb growth with an exponential saturation.

1. Introduction

Innovative DNA-based vaccines are currently under development [1–6] and aim to revolutionize the fight against diseases such as cancer, HIV, Ebola and Zika. These vaccines target antigen-presenting cells found in the dermis and epidermis, and therefore must be delivered into the intradermal (ID) region of the skin, which is known to promote a significantly enhanced immune response [7,8]. ID injection of low-viscosity vaccine by standard hypodermic needle and syringe (HNS) is typically achieved with the ‘Mantoux’ technique, which requires a highly skilled practitioner to insert a needle at a low angle relative to the skin. A successful injection into the ID region of the skin is typically characterized by a skin ‘wheal’, i.e. a raised circular area which has a blanched appearance [9,10]. In particular, a volume of 0.1 mL delivered into the ID region is expected to leave a skin wheal of approximately 6–10 mm[10]. However, based purely on this type of subjective visual inspection, one cannot estimate the amount of vaccine that was actually delivered into the correct region of the skin.

Furthermore, Mantoux injections (ID delivery with HNS) present significant drawbacks [11]; Firstly, the skin layers can be very thin, resulting in the potential of puncturing into the subcutaneous tissue, which may reduce the effective immune response of specific DNA-based vaccines [12–15]. Secondly, some of the vaccines developed for ID delivery are high-viscosity ($\mu \leq 200$ cP), so that use of a small diameter needle would create a large pressure drop along the needle ($\Delta P \propto \mu LQ/d^2$), therefore a substantial and sustained force is needed to dispense the drug from a syringe, making it difficult to hold a HNS in a fixed position. This was exemplified by a recent study [16] in which health-care workers overwhelmingly favored needle-free devices for ID delivery over HNS. Thus a needle-free approach for ID delivery should be pursued. Such an approach would also alleviate anxiety associated with HNS delivery [17–19], needle-stick injury treatment [20–22], and sharps waste in resource-limited environments [23–27].

High-velocity jet injection has a long history in both sub-cutaneous and intramuscular delivery [17,28]. The basic premise is that a high upstream pressure, created using either a spring or compressed gas mechanism, forces a jet at high-speed, $V_{jet} \sim O(100\ \text{m/s})$, from a narrow orifice, $D_0 \sim O(100\ \mu\text{m})$. Studies with both commercial and custom

---

* Corresponding author.
E-mail address: jeremy.marston@ttu.edu (J.O. Marston).

https://doi.org/10.1016/j.jconrel.2019.06.032
Received 18 February 2019; Received in revised form 14 May 2019
Available online 26 June 2019

devices in the literature [29–49] have comprised a combination of in-vitro [29–37], ex-vivo [38–44], and in-vivo [45–48] and primarily considered large doses (O(mL)) for SC and IM delivery, although some doses down to the nano-liter range have also been reported [49–51]. However, jet injection now also holds promise for intradermal delivery, as documented in clinical trials [16,52–55], and may overcome the drawbacks associated with Mantoux injection since the administrator subjectivity is removed as well as the possibility of delivering higher viscosity fluids. Yet it is still unclear whether jet injection can be tuned to exclusively deliver to the ID region.

To further advance jet injection for intradermal delivery, however, we must first understand mechanisms at play in the delivery stage and dispersion of the fluid within the dermal and, potentially, subcutaneous tissues. For intradermal delivery, the configuration of the injection can dramatically impact the efficacy of the delivery [28–43] and parameters such as stand-off (i.e. distance between the orifice and skin), skin tension and fluid properties play a key role, which will be discussed in detail in a separate publication. However, the specific aim of the present work is to provide a quantitative characterization of the bleb formation and elucidate the subtle differences between fluid viscosities. We therefore seek correlations between the delivered volume (measured by mass differential) and characteristic measurements of the injection site such as skin wheal diameter (above the skin), true bleb diameter (below the skin), and overall dispersion patterns (cross-sections). Based upon our analysis of over 700 injections, we propose that a visual inspection of the skin, as done for Mantoux injections, is insufficient to fully characterize intradermal injection.

2. Materials and methods

2.1. Injection device

The jet injector used in this study was the Bioject ID Pen, which is a streamline device originally designed for intradermal injection purposes. The device, shown in Fig. 1(a), comprises a spring housed in an upper chamber which is cocked by manually extending the arm on the outside of the chamber. A cartridge, shown in Fig. 1(b), pre-loaded with fluid is then inserted into the front end of the deivce and locked in place by rotation. The injection is then triggered manually by pressing on an external trigger ring, whereupon the spring is released and a piston hits the rear end of the plunger. After the injection, the used cartridge is released from position by pulling on a release ring.

The total volume expelled from the orifice during injection is $V_{ex} = 100\ \mu$L (0.1 mL), whilst the volume delivered into the skin, V, could be lower due to fluid rejection. The injection efficiency could therefore be stated as $E = 100 \times V_{ex}/V$. The upper cartridge inner diameter where the plunger travels is $D_p = 4.57$ mm, whilst the orifice diameter from where the jet exits is $D_j = 157 \pm 5\ \mu$m.

In clinical practice, an additional spacer attachement, featured in Fig. 1(b), can be fitted to the end of the cartridge. This serves to implement a stand-off distance, S, between the orifice and the skin. For our study, however, we varied the stand-off by removing the spacer ring and clamping the injector to an optical rail which could be moved vertically up and down, as shown in Fig. 2.

2.2. Fluid properties

For this study, water-glycerin mixtures with glycerin (LabChem Inc., Zelienople, PA, USA) concentrations of 0, 50, and 80%$_{w/w}$ were used to vary the fluid dynamic viscosity, which was determined using a stress-controlled protocol on a DHR3 rheometer (TA Instruments, New Castle, DE, USA) with a 40 mm, 0.017 rad cone-and-plate geometry. Multiple measurements for each fluid were performed at a constant temperature of 20 ^{o}C. The summary of fluids used and corresponding densities and viscosities are shown in Table 1. The fluid was dyed with Trypan blue dye (Sigma-Aldrich, concentration of 1 mg/mL) to aid image contrast and identify the injection region, but this did not have any noticeable effect on either density or viscosity. For each fluid, the average jet velocity at the orifice, V_j, was calculated from plunger displacement and mass conservation, and the corresponding jet power [41] is given by $P_j = \frac{\pi}{8}\rho D_j^2 V_j^3$. Both of these parameters are stated in Table 1.

2.3. Imaging

In order to obtain detailed jet dynamics and bleb growth, we employed high-speed video cameras (Phantom V1611, V711 and Miro M310) from Vision Research Ltd. (Wayne, NJ, USA). For most cases, a single side-view perspective was sufficient for the purposes of measuring total injection time and a qualitative overview. The cameras were operated at frame rates up to 100,000 fps, but typical video

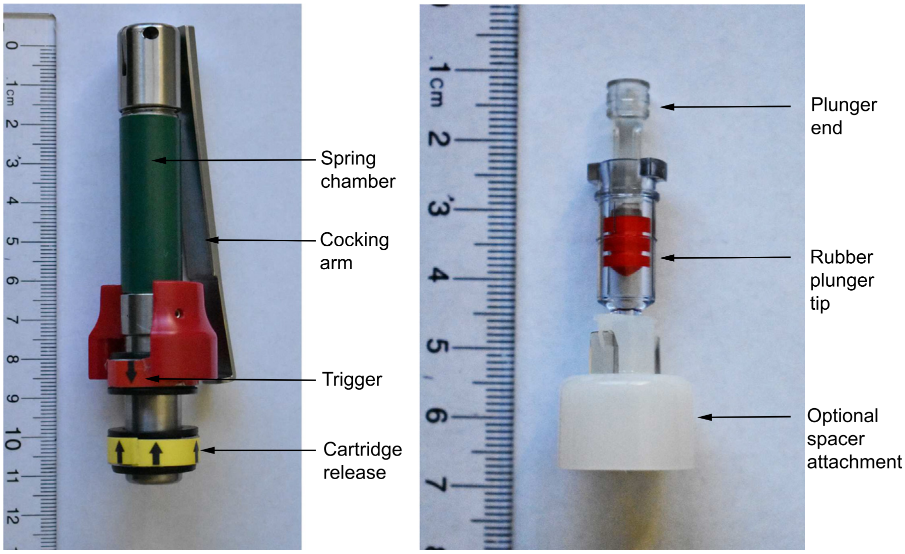

(a) (b)

Fig. 1. Photographs of (a) the ID Pen device and (b) standard cartridge for ejecting a volume of 0.1 mL. The white spacer attachment at the end of the cartridge featured in (b) is optional to create a stand-off distance of approximately 14 mm.

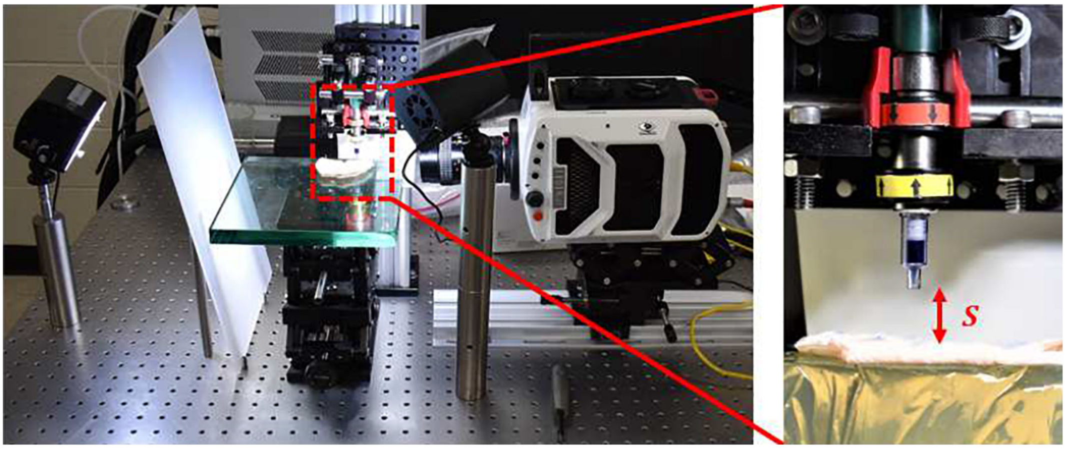

Fig. 2. Experimental setup showing the platform for the skin samples and jet injector configuration.

Table 1
Physical properties of the liquids used in the experiments. The glycerol mixtures are stated as concentration by volume ($\%_{v/v}$). Jet velocity and power correspond to an orifice diameter of $D_j = 157$ μm.

Liquid	Dynamic viscosity μ (Pa.s)	Density ρ (kg/m^3)	Jet velocity V_j (m/s)	Jet Power P_j (W)
DI water	0.001	996	126.7	19.61
50% glycerol	0.0069	1130	119.5	18.66
80% glycerol	0.084	1209	108.8	15.07

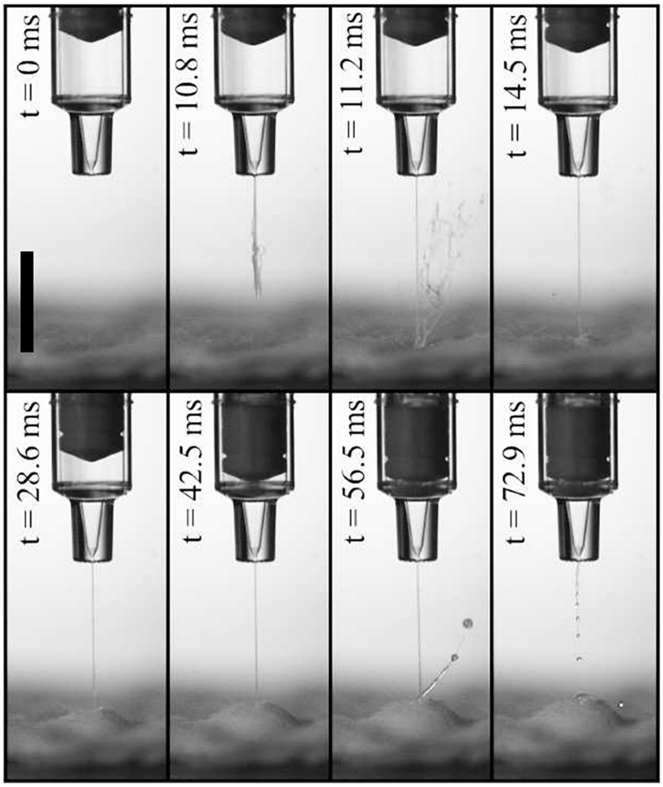

Fig. 3. Overview of the bleb formation during ex-vivo jet injection, facilitated by side-view high-speed videography. The guinea pig skin sample is placed approximately 14 mm below the orifice of the jet injector in this realization and the injection last 70 ms. The scale bar in the first image is 1 cm long and the video was captured at 14,000 fps.

sequences were captured at 57,000 fps. The temporal resolution is therefore ± 17.5 μs. In addition, using Nikon micro-nikkor 60 mm lenses with extension tubes, we achieved effective pixel sizes of between 16 and 50 μm/px. Post-injection, the skin samples were photographed with a Nikon D90 camera from the top, underside, and cross-sectional perspectives.

2.4. *Ex-vivo injections*

For this ex-vivo study, we used excised guinea pig skin taken from both the abdomen and flank regions of female Hartley guinea pigs from 20 to 52 weeks of age. The skin patches were approximately 8–10 cm long, 4–6 cm wide and had a thickness of 3–5 mm. Depending on the exact size of the skin sample, between 5 and 15 injections could be performed on a single sample. The skin was shaved prior to excision, but hair follicles remained for all samples. Guinea pig is a clinically relevant model, with similar characteristics in terms of strength thresholds at puncture to both human and porcine skin [56–59].

To ensure the skin surface was orthogonal to the jet, the skin sample was placed on a flat substrate and then positioned in the imaging setup (underneath the jet injector) shown in Fig. 2. The entire platform holding the skin could be moved vertically up or down using micrometer adjustment to achieve the desired stand-off distance, S, defined as the distance between the orifice and the upper skin surface. In this study, S was varied from 0 up to 16 mm.

In addition to different fluids and stand-off distances, the substrate beneath the skin sample was varied between a rigid glass plate, and a $5\%_{w/w}$ gelatin block, in order to assess the influence of the underlying tissue. Gelatin powder was purhcased from Sigma-Aldrich. The choice of a $5\%_{w/w}$ gelatin substrate was dictated by previous reports suggesting this approximately simulates soft tissue in humans [50,51]. The compliance of gelatin did lead to deformation under the force of the jet, which may change the angle of the skin relative to the incoming jet, however, over our range, we did not observe any statistical difference between the rigid (glass) backing and soft (gelatin) substrate in terms of volume delivered and bleb dimensions.

The skin mass was recorded prior to and after each injection (accuracy ± 0.1 mg) to deduce the mass, and thus volume of fluid injected in each trial. This was also verified by calculating the undelivered volume of fluid lost due to pooling (fluid remaining on top of the skin). We could therefore correlate the measured diameters and heights, as imaged from different perspectives (top, cross-section, underside) with the actual injected volume. In total, over 1000 injections were performed, of which 726 were used in the correlations. For clarity, we hereafter refer to raised skin at the injection site viewed from above (or side) as the 'wheal', whilst the fluid volume deposited within the dermal tissue is referred to as the 'bleb'. As such, the formation of a bleb in the dermal

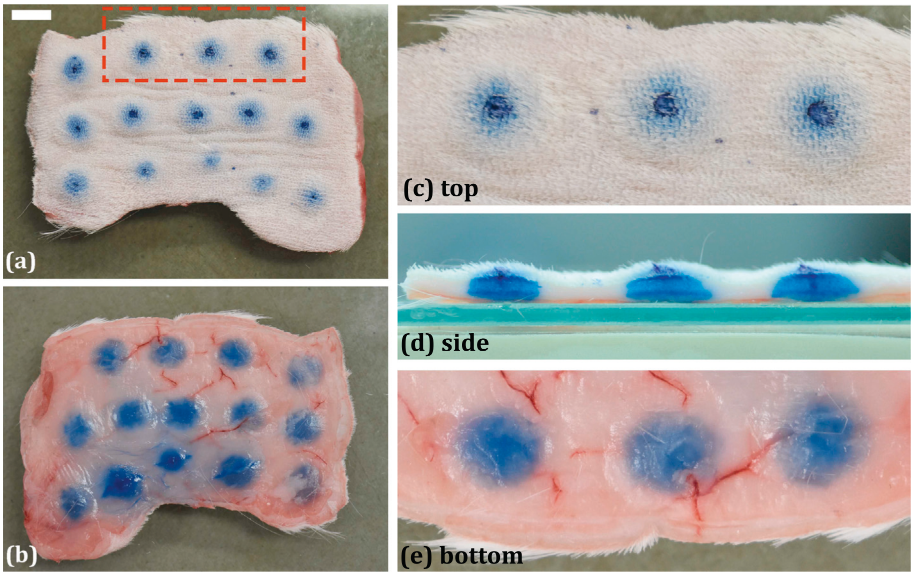

Fig. 4. (a) and (b): Front and back views of a guinea pig skin sample with a total of 14 skin blebs formed via jet injection of DI water with trypan blue dye. The stand-off distance was varied from $s = 8$ (top row) to $s = 4$ mm (middle row) to $s \approx 0$ mm (bottom row). The red dashed rectangle in (a) indicates the three blebs shown in the zoomed photographs in (c)-(e) for top, cross-section, and underside views respectively. The scale bar in (a) is 1 cm long.

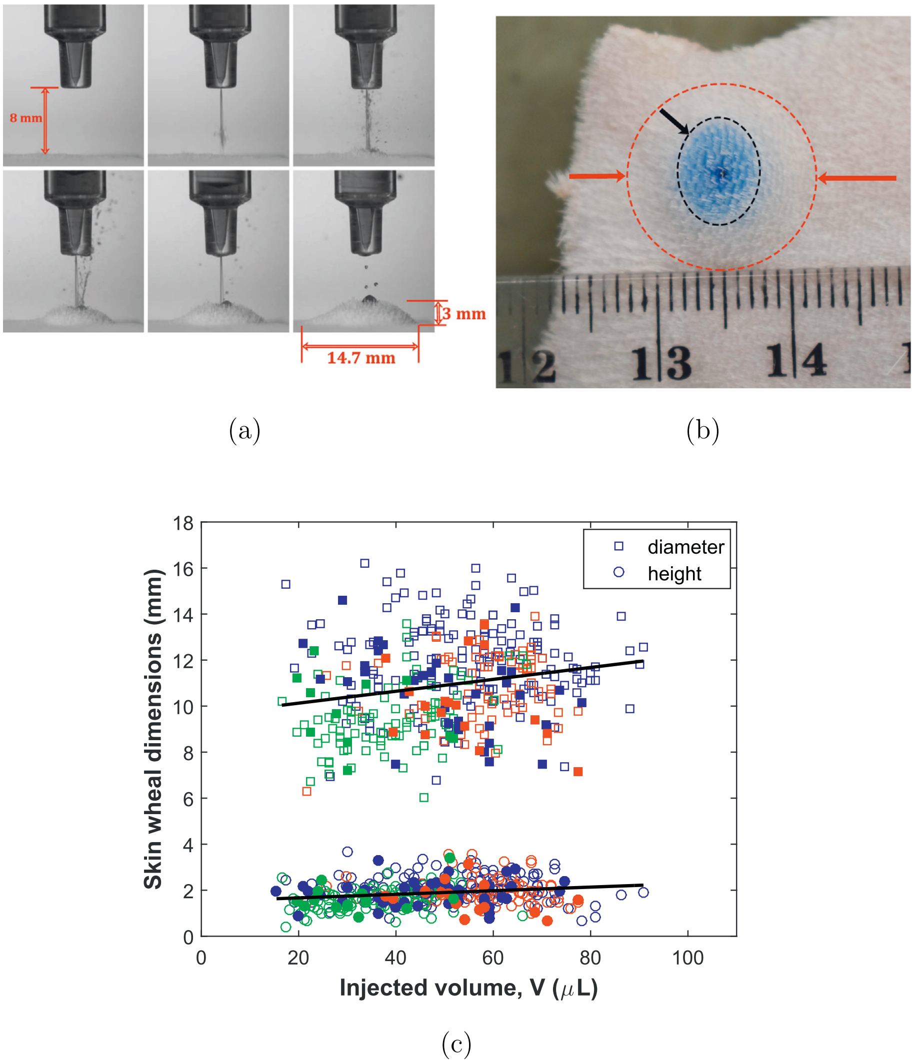

(a)

(b)

(c)

Fig. 5. (a) Side-view image sequence from a high-speed video of jet injection of water into guinea pig skin at a stand-off of $S = 8$ mm. The final bleb size is $d = 14.7$ mm and $h = 3$ mm. (b) Annotated top-view photograph of the skin wheal with ellipses marking the inner darkened region (black, $d \approx 7$ mm) and outer total extent (red, $d \approx 14.5$ mm). (c) Ensemble data ($n = 377$) showing both diameter (squares) and height (circles) against injected volume; Colors indicate different fluids (Blue = water, Red = 50% glycerin, Green = 80% glycerin); Open symbols represent glass backing, filled symbols indicate gelatin backing. The solid black lines indicate the best linear fits ($R^2 = 0.043$ in both cases). (For interpretation of the references to color in this figure legend, the reader is referred to the web version of this article.)

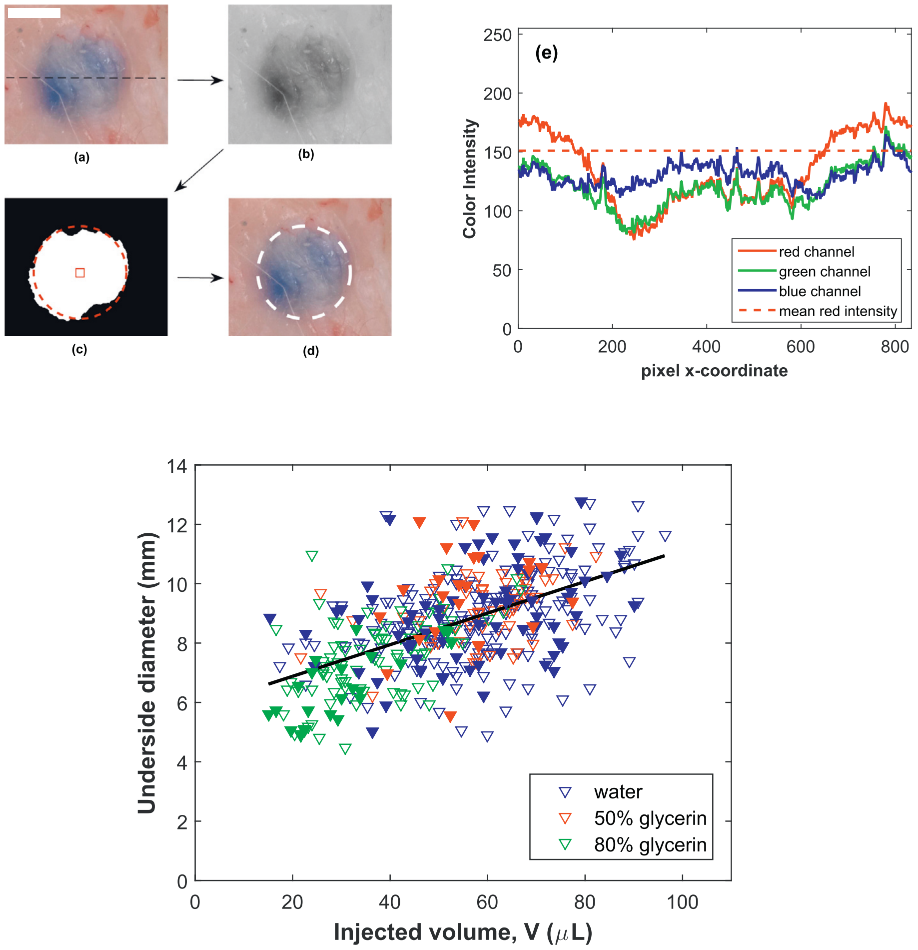

(f)

Fig. 6. Image analysis protocol on an isolated bleb from a photograph of the underside of the skin: (a) Original color image (scale bar 5 mm); (b) Red channel only; (c) binarized based upon red-channel filter; (d) circular equivalent diameter (9.5 mm) marked on the original image; (e) Color intensities along a single pixel line indicated by the dashed line in image (a). The ensemble data for the bleb diameters measured using this method is shown in (f), with the best linear fit shown by the solid black line ($R^2 = 0.31$). (For interpretation of the references to color in this figure legend, the reader is referred to the web version of this article.)

layers results in a raised skin wheal. After injection, the skin samples were photographed from above and the underside, then sectioned medially (across the jet puncture site) with a sharp blade to view the cross-section.

3. Results and discussion

3.1. Overview of the jet injection process

Fig. 3 presents an overview of a typical ID jet injection process (ex-vivo) into excised guinea pig skin. The select images taken from a high-speed video sequence indicate the principal stages of the injection as follows: (i) Initial configuration prior to triggering device. (ii) Jet formation. (iii) Jet impact on skin and splashing. (iv) Jet penetration into dermis. (v) Fluid accumulation in the ID region and formation of a skin bleb. (vi) Jet deceleration and end of injection. (vii) Jet break-up and final bleb state. The total jetting time depends upon the fluid viscosity, but typically lasts between 30 and 80 ms. During the jet 'start-up' phase ($t \lesssim 1$ ms) the impulsive action of the spring-piston causes a rapid pressure rise in the liquid inside the cartridge and a very high velocity jet, ($O(300)m/s$), impacts and punctures the skin. After this, the plunger achieves a linear motion, which is considered the 'steady-stream' phase, with a velocity of $V_j \sim O(100)$ m/s and a flow rate, $Q \sim 2 \times 10^{-6}$ m^3/s (120 mL/min). The impact of the jet exerts a pressure, $p \sim \rho V_j^2$, on the skin across an area assumed to be roughly equal to that of the orifice, $A \approx \pi D_j^2/4$, yielding impact forces of $F = pA \sim O(10^{-1})$N.

In addition to side-view videos, the skin samples are photographed to render both top-view perspectives, akin to a visual inspection of the skin wheal, underside and cross-sectional views, as exemplified in Fig. 4; here we present full-width photographs (a and b) of the top and underside of a guinea pig skin sample, and close-up photographs (c-e) of the top, cross-section, and underside views, respectively. From each of these perspectives, we measure the diameter, however the cross-sections also provide the true total depth of the bleb relative to the top of the skin.

3.2. Top-view measurements of the skin wheal

As stated earlier, clinical practice relies upon visual confirmation of the presence of a skin wheal, viewed from above. In our experiments, the wheal is clearly observed in both the high-speed video (side-view) and the top-view photographs following the injection, as evidenced in Fig. 5. In this particular realization, the injection of water occurs from a stand-off of 8 mm and results in a wheal diameter, $d \approx 14.7$ mm, and height, $h \approx 3$ mm. The image sequence in 5(a) shows the temporal evolution, whilst the photograph in 5(b) shows the final state next to a millimetric scale. The total extent of the skin wheal measured from the top-view ($d \approx 14.5$ mm) corresponds to the side-view from the high-

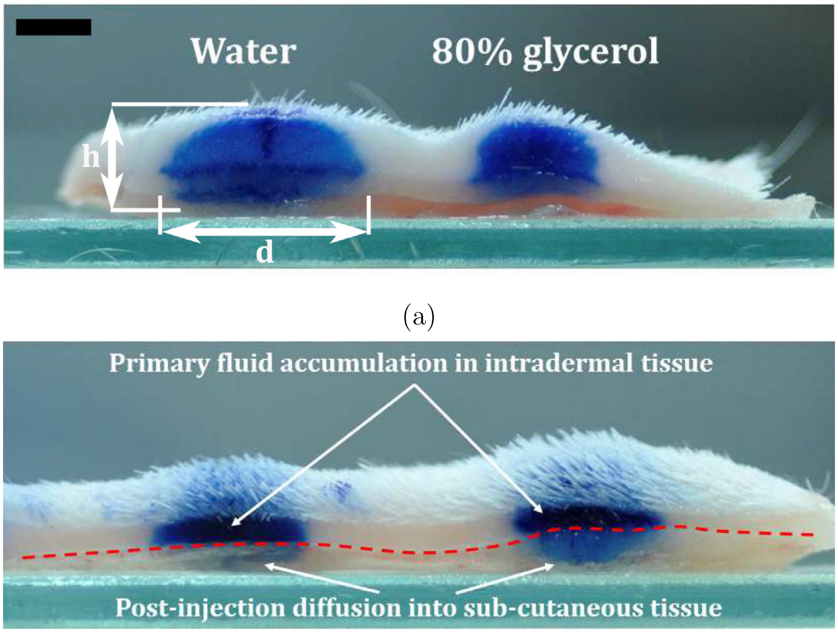

(a)

(b)

Fig. 7. (a) Cross-sections of water and 80% glycerol blebs in the same skin sample from a stand-off distance of 4 mm, with corresponding injection volumes of 0.069 and 0.047 mL. The scale bar is 5 mm long (b) Cross-sections showing the primary fluid accumulation site, i.e. true blebs as indicated by dark blue regions, and post-injection diffusion into subcutaneous tissue (below the red dashed line) as indicated by faint blue regions. The red dashed line represents the demarcation between the dermis and subcutis. (For interpretation of the references to color in this figure legend, the reader is referred to the web version of this article.)

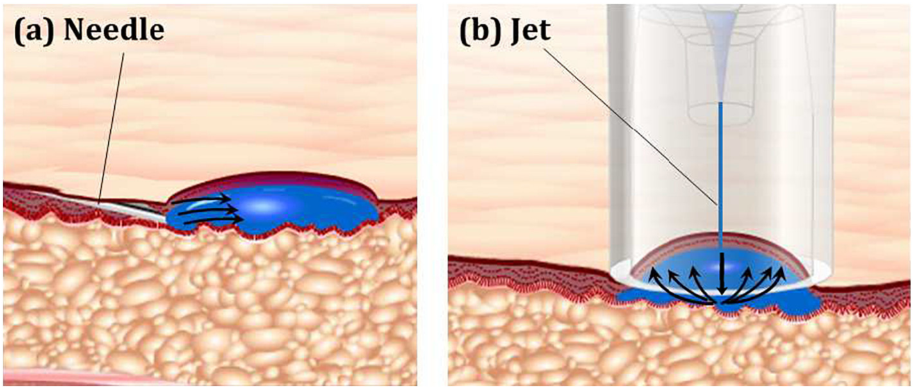

Fig. 8. Schematic representation of fluid flow patterns (black arrows) in both needle-based (a) and jet-based (b) intradermal injections.

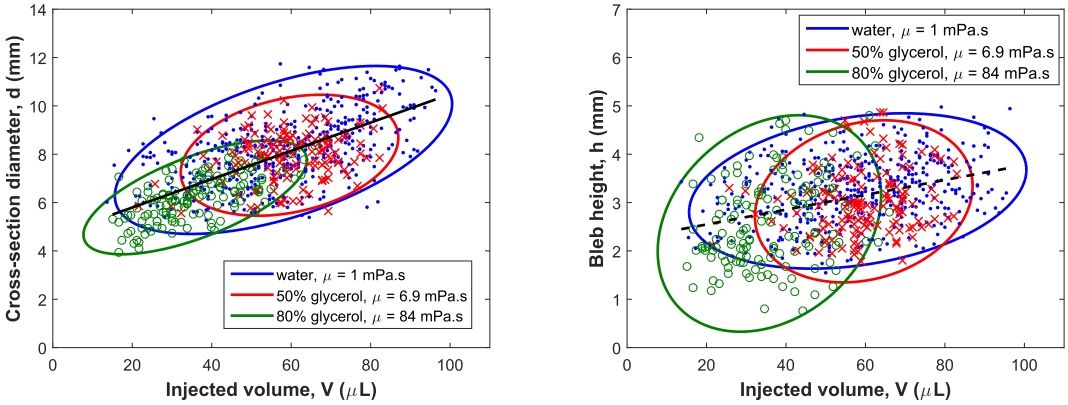

(a)

(b)

Fig. 9. Ensemble data of (a) bleb diameters, and (b) bleb heights versus injected volume for different fluid viscosities: water ($\mu = 1$), 50% glycerol ($\mu = 6.9$), and 80% glycerol ($\mu = 84$). The ellipses correspond to 95% confidence ellipses. Total number of data points for water, 50% glycerol, and 80% glycerol were $n = 446$, 143, and 137, respectively. The solid black lines represents the best linear fits to the ensemble data with correlation coefficients of $r^2 = 0.48$ ($RMSE = 1.14$, $MNE = 11.9\%$) and $r^2 = 0.16$ ($RMSE = 0.72$, $MNE = 22.3\%$).

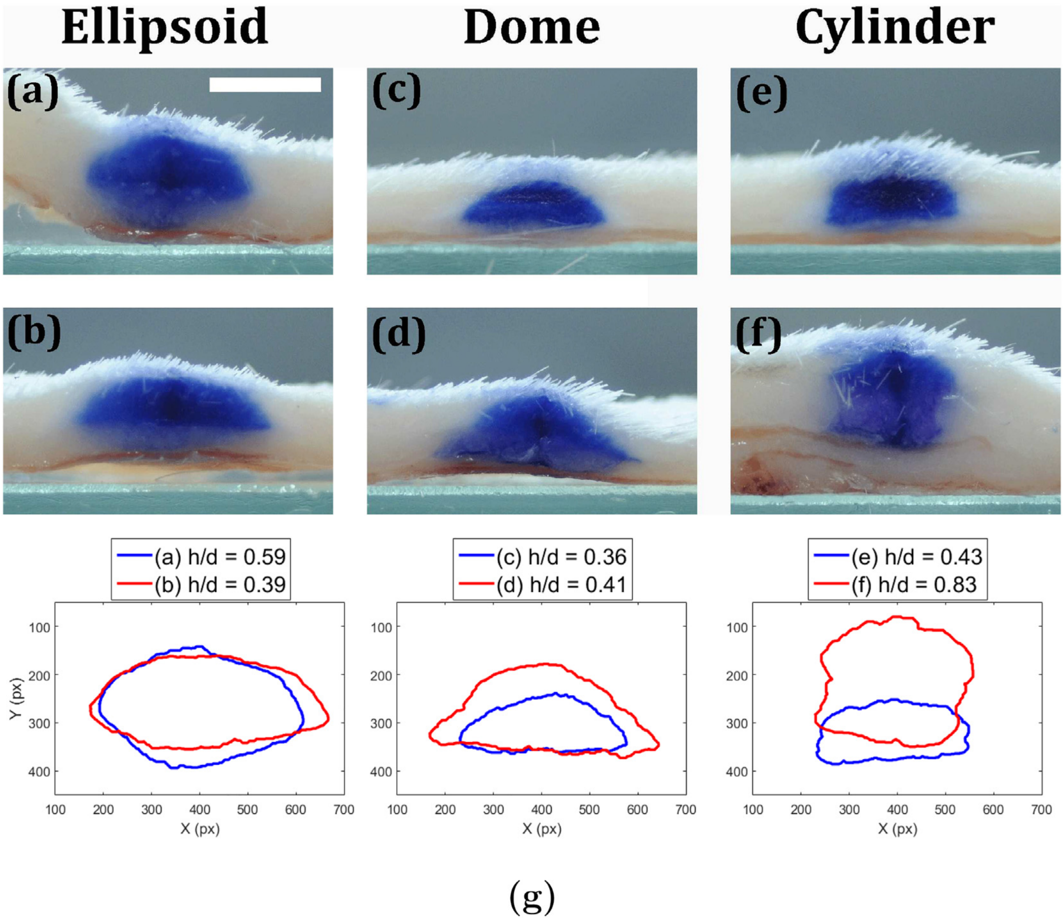

Fig. 10. Catalog of bleb shapes observed, classified by their approximate shapes as ellipsoid (a,b), dome (c,d), and cylinder (e,f). All blebs shown were formed from 50% glycerol with standoffs of 8 mm (a,b) and 14 mm (c,d,e,f). The digitized outlines are shown in (g) along with the aspect ratios, *h/d*. The scale bar in (a) is 5 mm long and applies to all images.

speed video, indicating that within the time-frame of the experiment, diffusion into the skin is negligible. However, we also observe that there is a concentrated inner region ($d \approx 7$ mm, marked by the black ellipse), which is an indication of an elliptical- or dome-shaped dispersion pattern under the skin.

By extracting the skin wheal dimensions across the entire data set where side-view and top-view measurements were made, we can assess whether any true quantitative trends exist. Fig. 5(c) plots this data for both the diameter and height of the skin wheal against injected volume. Here, we have shown data for all three fluids and both substrate types (glass with open symbols and gelatin with filled symbols). We observe that despite achieving a range of injection volumes from approximately 20–90 μL, there is a broad range of skin wheal diameters and heights that could result from any given volume. For example, with $V \approx 60$ μL, the apparent skin wheal diameter could range from 8 mm up to nearly 16 mm. As such, there is no statistical significance between the substrates and there is no correlation between the skin wheal dimensions and injected volume ($R^2 = 0.043$).

In summary, a raised skin wheal, as per a simple visual inspection, is indicative of a fluid deposit in the dermal tissues but, given the lack of correlation observed herein, the skin wheal alone cannot be used to determine quantitative information of the precise volume deposited into the ID region.

3.3. Underside-view of the skin bleb

Specific to the underside view, as shown in Fig. 4 (b) and (e), this view requires color-based image analysis due to the diffuse nature of the edges, exemplified by Fig. 6, for the same bleb shown in Fig. 5. In brief, we crop a region of interest around the bleb (image (a)) and filter just the red channel (image (b)). The rationale for this is that the red channel shows the greatest variation because in the digital images red is suppressed in the regions where the blue dye is most concentrated - this is shown graphically in 6(e), which presents the red, blue and green intensities along a line-scan (indicated by the black dashed line in image (a)). We find that the edge of the bleb can be well-approximated by thresholding when the red channel intensities fall below the mean red intensity across the whole image (red dashed line in (e)). Using this filter, the image is then binarized and the centroid and circular equivalent can be easily deduced (see image (c)). The circular outline of the bleb is then overlayed on the original raw image (image (d)), which provides a good visual match. This procedure results in an underside diameter of 9.5 mm, which is clearly smaller than the diameter of the top-view measurement ($d = 14.7$ mm) of the skin wheal, again indicating some kind of elliptical pattern. Compiling the ensemble data across both substrates and fluids, we present the diameter as a function of injected volume in Fig. 6(f). This plot does indicates a positive correlation, however, we again find that the correlation is weak with $R^2 = 0.31$. This further reinforces the need to assess the full dispersion pattern, which can only be garnered through the cross-sectional perspective. As such, we proceed for the remainder of the analysis with the cross-sectional measurements of the bleb.

3.4. Cross-section measurements

For cross-section measurements, the skin samples are sectioned

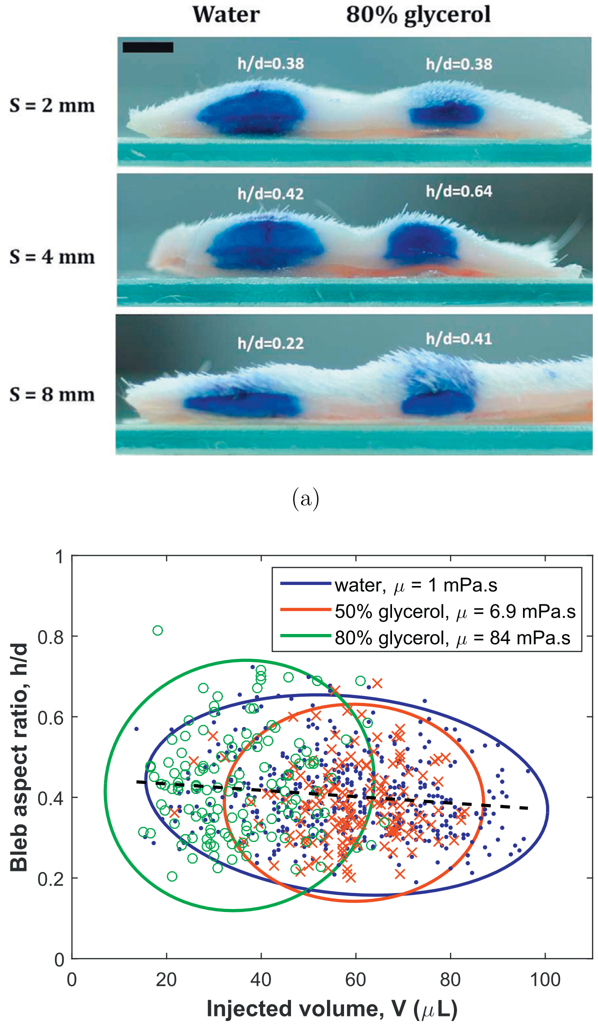

(a)

(b)

Fig. 11. (a) Cross-section images of adjacent skin blebs for water and 80% glycerol in the same skin sample, annotated with aspect ratios (*h*/*d*). The standoff is indicated to the left of the images and the scale bar in the top image is 5 mm long. (b) Ensemble comparison of bleb aspect ratios versus injected volume for the same data as Fig. 9: water ($\mu = 1$), 50% glycerol ($\mu = 6.9$), and 80% glycerol ($\mu = 84$). The ellipses correspond to 95% confidence ellipses, whilst the black dashed line represents the best linear fit across all data sets.

medially and photographed. We then take the maximum diameter of the bleb, *d*, along with the depth of the bleb, *h*, as shown in Fig. 7(a). Interestingly, these cross-section images reveal that the maximum lateral spread largely coincides with the boundary between the dermis and subcutis (see Figs. 7 a & b); We hypothesize that this is because the jets penetrate down to this boundary and spread laterally, shown schematically in Fig. 8. As such, the fluid from the jet stream must disperse both radially (outward) and vertically (upward) from the site of deepest penetration, which represents a fundamental difference from needle-based (Mantoux) injections, whereby the inejction depth is set by the needle and bevel orientation. For the majority of cases we found the lowermost extent of the bleb to be readily ascertained, such as Fig. 7(a), which appeared to coincide with the boundary of tissue layers (distinguished by change in color). However, in some cases, the lowermost extent was not so easily determined, due to fluid diffusion into the subcutis post-injection (see Fig. 7b). In such cases, depth of the bleb is defined as the distance from the top of the skin down to the lowest part of the dark blue region.

In contrast to the top and underside views, the measurements from medial-sectioning (i.e. cross-sections) of the bleb diameters do provide a favorable positive correlation, as shown by the ensemble data ($n = 726$) in Fig. 9(a), and is consistent across all fluid viscosities. In this plot, we show all the individual data points along with the 95% confidence ellipses for each fluid. For a guide to the overall trend, the best linear fit encompassing all data is shown by the solid black line ($r^2 = 0.48$). From a quick visual inspection of the data, it is immediately obvious that all fluids follow a similar correlation, however, some subtle differences are also apparent; First, we note that increasing the viscosity from 1 to 6.9 mPa.s results in approximately the same mean injection volume and bleb diameter ($\overline{V} \approx 60\mu$L, $\overline{d} \approx 8$ mm), but also leads to a more consistent injection - this is clear by examining the magnitude of the confidence ellipses for these respective fluids. Second, we observe that increasing the viscosity to 84 mPa.s leads to a qualitative difference - a reduced mean injection volume, but also a more consistent injection, i.e. less scatter in terms of bleb diameter, which can be verified by observing that the ellipse minor axis is significantly smaller.

With regards to depth of the injection, the maximum penetration depth for such ex-vivo experiments is limited by the thickness of the skin sample. However, we found that the majority of injections only penetrated down to the boundary of the dermis and subcutaneous tissue; This means that, as sketched in Fig. 8, the bleb fills both laterally and vertically upward from this depth. The bleb height, however, displays more scatter than the diameter, as evidenced by the data in Fig. 9(b). Here, we observe that the correlation is much weaker than for the diameter ($r^2 = 0.16$), and specific to the highest viscosity, there is a much broader confidence ellipse, meaning a signifcantly broader range of heights. We emphasize that the measured dimensions in Fig. 9 should not used to infer volume delivered - this comes directly from measurement of the rejected fluid. Rather, the purpose here is to find a correlation and range of most likely values of height and diameter for a *known* volume, the effect of diffusion notwithstanding. This is important to help guide design of electroporation modules, where electric field coverage is a key consideration.

Overall, the data indicates that the best correlation is provided by the cross-sectional bleb views, and that the top-view perspective of the skin wheal alone does is insufficient to characterize the injection. Whilst the ensemble data (spanning 726 injections) presented in Fig. 9 provides a general overview as to the effect of viscosity on injection efficiency and bleb diameter and height, it does not provide details into the shape of the blebs (e.g. elliptical, conical, aspect ratios). As such, it is instructive to look more closely at the influence of viscosity on bleb shapes.

With regards to injection efficiency and delivered volume, Fig. 9 indicates that there may exist optimal volumes in order to maximize the efficiency (i.e. minimize fluid rejection form the skin). For water and 50% glycerol, this value is $V_{ex} \approx 60 - 70$ μL, whilst for 80% glycerol, the corresponding value is $V_{ex} \approx 40$ μL.

3.5. Bleb shape

In terms of shape, visual inspection indicates that all the blebs are oblate, i.e. the diameter exceeds the depth, as seen in Figs. 4 and 7. In addition to this, we can also observe a variation in the shape, which loosely fall into three catergories - ellipsoid, dome, and cylinder. These are depicted by the cross-section photographs in Fig. 10, where the images were specifically chosen to exemplify the variation within each of the three catergories. Below each pair of images is the digitally extracted outline (from color image thresholding) along with the height-to-diameter aspect ratio, *h*/*d*. Whilst this aspect ratio does not qualify the overall shape, it does provide a single quantifier of the horizontal vs. vertical spread of the fluid. As such, by examining the aspect ratio, *h*/*d*, across the full spectrum of data, we can discern the effect of viscosity on shape.

With this in mind, Fig. 11(a) presents photographs of both water

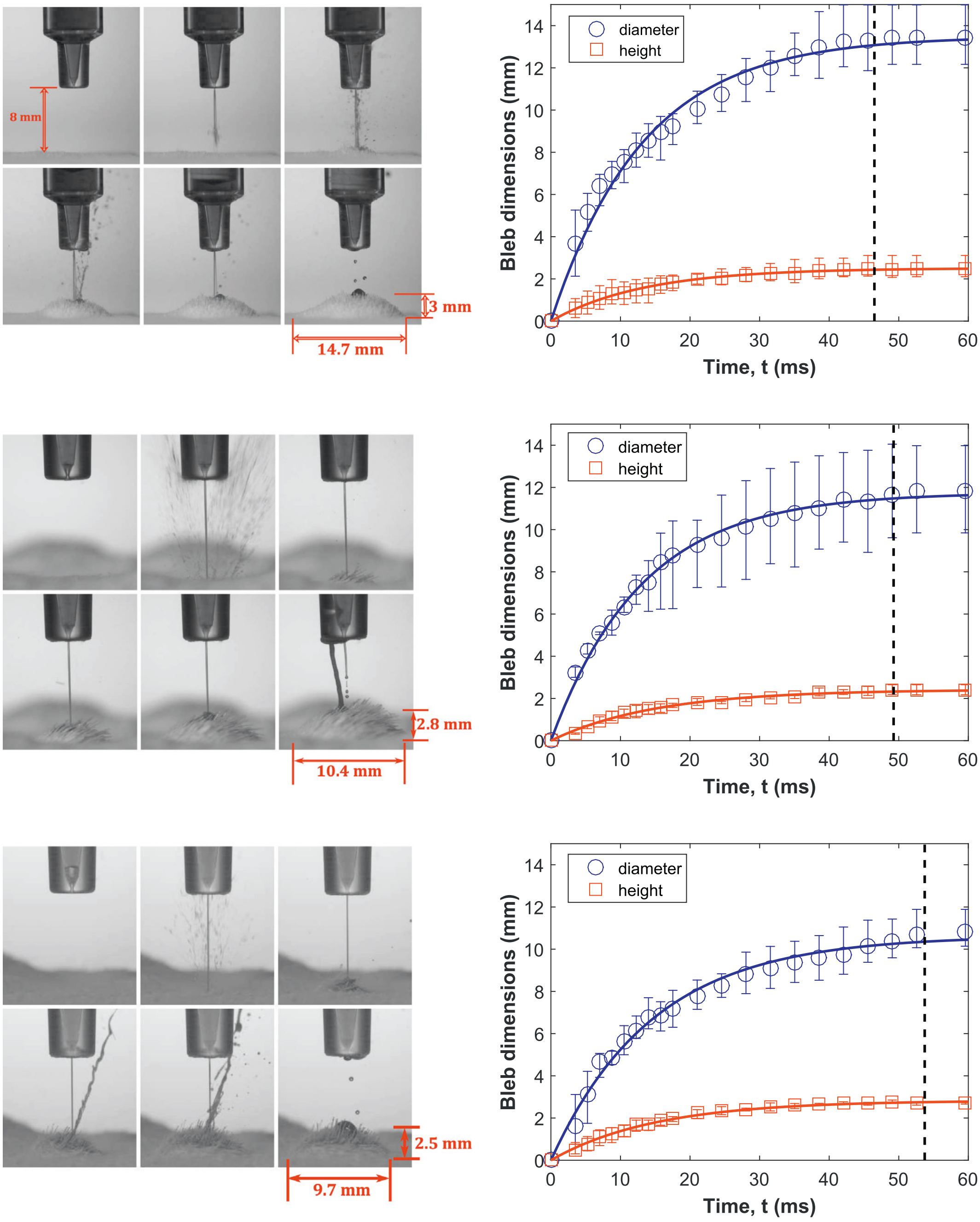

Fig. 12. High-speed video sequences for injection of (a) water, (b) 50% glycerol, and (c) 80% glycerol, all with $S = 8$ mm. (d)-(f): Corresponding temporal growth (diameter and height), averaged over five trials. The solid lines in each plot represent the best fit using an exponential saturation model, $d(t) = d_{max}(1 - e^{-kt})$, whilst the vertical dashed lines correspond to the approximate end of the jet.

and 80% glycerol for different standoffs, where each adjacent pair was injected into the same skin patch. Whilst standoff distance between 2 and 8 mm does not have a significant effect over this range of viscosity, the consistent observation is that water spreads further horizontally and forms more oblate shapes. The full quantitative evaluation of bleb shapes is summarized in Fig. 11(b), which plots the aspect ratio versus volume for the same data range as Fig. 9. Again, for a single quantitative statistical measure, we plot the 95% confidence ellipses for each fluid, which indicates that both water and 50% glycerol blebs are the most oblate with mean aspects ratios of approximately 0.4, ($\overline{h/d} \approx 0.38$) around an injection volume of 60 μL, whilst 80% glycerol has a mean aspect ratio of 0.42 around 35 μL but with more significant variation (noted by the almost circular confidence ellipse). From this, we infer that the lower viscosity fluids spread laterally to form more elongated dome-shaped or elliptical-shaped blebs than higher viscosity fluids. For the 80% glycerol, whilst the blebs are still oblate, they do not spread laterally to the same degree as the low-viscosity fluids. This could be a confluence of both different filling patterns during the timescale of injection, and post-injection diffusion which would be more significant for low viscosity fluids This could have important implications for the design of post-injection trafficking devices, such as electroporation modules [12–14], which are designed to apply electrical current throughout the bleb volume, to maximize the total number of transfected cells.

3.6. Injection dynamics

As a final observation from the high-speed video sequences, we assess the temporal growth rate of the skin wheal across the timescale of the injection. Figs. 12(a)-(c) present example sequences for the three fluids from which these measurements are extracted. In each sequence, the stand-off was $S = 8$ mm, and the final diameter and height are shown in the last image. As we can see from the images, there is some initial fluid loss due to splashing and fluid rejection in the latter stages, however, we also see a qualitative similarity in the evolution, in that the wheals grow rapidly in the early stage, and more slowly toward the end of the injection. This is more easily seen in the data plots in 12(d)-(f), which plot the diameter and height versus time, averaged over five trials, where each trial resulted in an injection volume $V \approx 40$ μL.

Despite the differences in final size of the skin wheals, the growth dynamics are qualitatively similar in that there is an initial rapid increase in diameter and height for $t \lesssim 20$ ms, followed by a slower approach to the maximum for $t \gtrsim 20$ ms. From a purely heuristic standpoint, this type of growth can be modeled with an exponential saturation function, $d(t) = d_{max}(1 - e^{-kt})$, where d_{max} is the final (maximum) diameter and k is rate constant. The best fits to the data using this function, for both diameter and height, are shown in each plot by the solid lines. The vertical dashed lines mark the approximate end of the jetting, at which point the skin wheal growth stops, and largely coincide with the saturation point of the curves. From these data sets, we note that the diameter appears inversely correlated with viscosity, whilst the height increases with viscosity, which is consistent with the quantitative trends seen in Fig. 11.

This non-linear evolution indicates that the intrusion of fluid into the intradermal tissue occurs in a complex fashion, which is determined by an intricate interplay between the incoming flow rate, fluid viscosity, and the counter-pressure build-up due to the elastic response within the tissue. Previous reports of intradermal and subcutaneous injections found that the counter-pressure can be as high as 500 kPa [9,60], which means that there could be significant resistance as the incoming jet stream spreads laterally within the skin. As the fluid viscosity increases, the jet flow rate decreases accordingly (see Table 1), which could further limit the bleb growth in the latter stages. We postulate that this could be the cause of the fluid rejection observed in the videos.

4. Conclusions

In summary, we have conducted a study of intradermal jet injection into ex-vivo guinea pig skin with the principal aim of elucidating the effect of viscosity on dispersion patterns, and metrics to quantify the shapes of the blebs formed. The nozzle orifice diameter used was 157 μm and, with fluid viscosities from 1 to 84 mPa.s, the resulting jet velocities ranged from 109 to 127 m/s, which was sufficient to penetrate the skin.

Our quantitative data analysis showed that there was no correlation between the dimensions of the skin wheal (viewed from above the skin) and the injected volume, and only a weak correlation between the diameter measured from below the dermis and injection volume. In contrast, medial sectioning revealed a moderate-strength postitive correlation between the cross-sectional diameter of the bleb and the injected volume. This indicates that a top-view visual inspection, currently used in the clinic [10,16] to evaluate the success of intradermal delivery, is insufficient to fully characterize the injection.

The injection dynamics were quantified by assessing the temporal bleb growth, and it was found from a heuristic standpoint, that the bleb growth could be described with an exponential saturation. This functional form captures the qualitative observation of fluid rejection in the high-speed video, and suggests that the counter-pressure build-up in the dermal tissue can be sufficient to overcome the fluid flow from the jet in the latter stages of injection.

A key finding in our study is that viscosity plays a dominant role in determining the injected volume and dispersion pattern, the fluid velocity notwithstanding. This presents a challenge going forward for intradermal delivery of vaccines that may be more viscous than water with regards to how to increase injection efficiency. Furthermore, the higher-viscosity fluids tend to spread less laterally, forming a more cylindrical-shaped bleb, whereas low-viscosity fluids have a higher degree of lateral dispersion. This highlights the need for a deeper understanding of the fluid dynamics at play in both jet creation (i.e. upstream of the orifice), jet impact, and fluid-structure interaction within the dermal layers. These aspects will be addressed in detail in forthcoming publications. In addition, a recent study highlighted the influence of jet shape on injection patterns [61], thus extending this study to ID delivery will also be of interest. Lastly, future efforts could also address the effect of freeze-thawing on the fluid dispersion measurements.

Acknowledgements

This work was financially supported by Inovio Pharmaceuticals, United States of America and The National Science Foundation, United States of America via award number NSF-CBET-1749382.

References

[1] M.A. Liu, DNA vaccines: a review, J. Intern. Med. 253 (2003) 402–410.
[2] M.A. Kutzler, D.B. Weiner, DNA vaccines: ready for prime time? Nat. Rev. Genet. 9 (2008) 776–788.
[3] J. Rice, C.H. Ottensmeier, F. Stevenson, DNA vaccines: precision tools for activating effective immunity against cancer, Nat. Rev. Cancer 8 (2008) 108–120.
[4] S.S.A.A. Hasson, J.K.Z. Al-Busaidi, T.A. Sallam, The past, current and future trends in DNA vaccine immunizations, Asian Pacific J. Top. Biomed. 5 (2015) 344–353.
[5] J.K. Vasir, V. Labhasetwar, Targeted drug delivery in cancer therapy, Tech. Cancer Res. Treat. 4 (2005) 363–374.
[6] www.inovio.com/products/ (accessed May 2019).
[7] J.-F. Nicolas, B. Guy, Intradermal, epidermal and transcutaneous vaccination: from immunology to clinical practice, Expert Rev. Vaccines 7 (2008) 1201–1214.
[8] P.H. Lambert, P.E. Laurent, Intradermal vaccine delivery: will new delivery systems transform vaccine administration? Vaccine 26 (2008) 3197–3208.
[9] J. Gupta, S. Park, B. Bondy, E.I. Felner, M.R. Prausnitz, Infusion pressure and pain during microneedle injection into skin of human subjects, Biomaterials 32 (2011) 6823–6831.
[10] C.C. Dasco, Skin testing for tuberculosis, in: Walker, Hall & Hurst (Ed.), Clinical Methods: The History, Physcial and Laboratory Examinations, Butterworths, 1976.
[11] J. Hickling, R. Jones, Intradermal delivery of vaccines: a review of the literature and the potential for development for use in low- and middle-income countries, WHO Report, 2009.
[12] K.E. Broderick, A.S. Khan, N.Y. Sardesai, DNA vaccination in skin enhanced by electroporation, Methods Mol. Biol. 1143 (2014) 123–130.
[13] J.B. McCoy, J.M. Mendoza, K.W. Spik, C. Badger, A. Gomez, C.S. Schmaljohn, N.Y. Sardesai, K.E. Broderick, A multi-head intradermal electroporation device allows for tailored and increased dose DNA vaccine delivery to the skin, Hum. Vaccine Immunother. 3 (2014) 10.
[14] K.E. Broderick, L.M. Humeau, Electroporation-enhanced delivery of nucleic acid vaccines, Expert Rev. Vaccines 14 (2015) 195–204.
[15] M.R. Prausnitz, A practical assessment of transdermal drug delivery by skin electroporation, Adv. Drug Deliv. Rev. 35 (1999) 61–76.
[16] S. Resik, A. Tejeda, O. Mach, C. Sein, N. Molodecky, C. Jarrahian, L. Saganic, D. Zehrung, M. Fonesca, M. Diaz, N. Alemany, G. Garcia, L.H. Hung, Y. Martinez, R.W. Sutter, Needle-free jet injector intradermal delivery of fractional dose inactivated poliovirus vaccine: association between injection quality and immunogenicity, Vaccine 33 (2015) 5873–5877.
[17] S. Mitragotri, Current status and future prospects of needle-free liquid jet injectors, Nat. Rev. Drug Discov. 5 (2006) 543–548.
[18] Y. Nir, A. Paz, E. Sabo, J. Potasman, Fear of injection in young adults: prevalence and associations, Am J. Trop. Med. Hyg. 68 (2004) 341–344.
[19] C.M. McMurty, M. Noel, A. Taddio, M.M. Antony, G.J.G. Asmundson, R.P. Riddel, C.T. Chambers, V. Shah, Interventiona for individuals with high levels of needle fear: systematic review of randomized controlled trials and quasi-randomized controlled trials, Clin. J. Pain 31 (2015) S109.
[20] M. Kakizaki, N. Ikeda, M. Ali, B. Enkhtuya, M. Tsolmon, K. Shibuya, C. Kuroiwa, Needlestick and sharps injuries among healthcare worker at public tertiary hospitals in an urban community in Mongolia, BMC Res. Notes 4 (1) (2011) 184.
[21] The World Health Report, Reducing Risks, Promoting Healthy Life, 2002.
[22] A. Mannocci, G. De Carli, V. Di Bari, R. Saulle, B. Unim, N. Nicolotti, L. Carbonari, V. Puro, G. La Torre, How much do Needlestick injuries cost? A systematic review of the economic evaluations of needlestick and sharps injuries among healthcare personnel, Infect. Control Hosp. Epidemiol. 37 (2016) 635–646.

[23] M. Saia, F. Hoffman, J. Sharman, D. Abiteboul, M. Campins, J. Burkowitz, Y. Choe, S. Kavanagh, Needlestick injuries: incidence and cost in the United States, United Kingdom, Germany, France, Italy, and Spain, Biomed. Int. 1 (2) (2010) 41–49.
[24] L. Jodar, P. Duclos, J.B. Milstein, E. Griffiths, M.T. Aguado, C.J. Clements, Ensuring vaccine safety in immunization programmes - a WHO perspective, Vaccine 19 (2001) 1594–1605.
[25] Proceedings of the Annual Meeting of the Safe Injection Global Network, Dubai, (2010).
[26] Assessment report of the Global Vaccine Action Plan, (2014).
[27] Secretariat Annual Report of the Global Vaccine Action Plan: Monitoring, Evaluation and Accountability, (2016).
[28] R.A. Hingson, J.G. Hughes, Clinical studies with jet injection: a new method of drug administration, Curr Res. Anesth. Analg. 26 (1947) 221–230.
[29] J. Schramm-Baxter, J. Katrencik, S. Mitragotri, Jet injection into polyacrylamide gels: investigation of jet injection mechanics, J. Biomech. 37 (2004) 1181–1188.
[30] R.F. Donnelly, D.I.J. Morrow, P.A. McCarron, M.J. Garland, A.D. Woolfson, Influence of solution viscosity and injection protocol on distribution patterns of jet injectors: application to photodynamic tumour targeting, J. Photochem. Photobiol. B 89 (2007) 98–109.
[31] A. Arora, M.R. Prausnitz, S. Mitragotri, Micro-scale devices for transdermal drug delivery, Int. J. Pharm. 364 (2008) 227–236.
[32] J.C. Stachowiak, T.H. Li, Anubhav Arora, S. Mitragotri, D.A. Fletcher, Dynamic control of needle-free jet injection, J. Control. Release 135 (2009) 104–112.
[33] J.C. Stachowiak, M.G. von Muhlen, T.H. Li, L. Jalilian, S.H. Parekh, D.A. Fletcher, Piezoelectric control of needle-free transdermal drug delivery, J. Control. Release 124 (2007) 88–97.
[34] T.M. Grant, K.D. Stockwell, J.B. Morrison, D.D. Mann, Effect of injection pressure and fluid volume and density on the jet dispersion pattern of needle-free injection devices, Biosyst. Eng. 138 (2015) 59–64.
[35] X. Li, B. Ruddy, A. Taberner, Characterization of needle-assisted jet injections, J. Control. Release 243 (2016) 195–203.
[36] A. Schoubben, A. Cavicchi, L. Barberini, A. Faraon, M. Berti, M. Ricci, P. Blasi, L. Postrioti, Dynamic behavior of a spring-powered micronozzle needle-free injector, Int. J. Pharm. 491 (2015) 91–98.
[37] O.A. Shergold, N.A. Fleck, T.S. King, The penetration of a soft solid by a liquid jet, with application to the administration of a needle-free injection, J. Biomech. 39 (2006) 2593–2602.
[38] N. Inoue, H. Todo, D. Iidaka, Y. Tokudome, F. Hashimoto, T. Kishino, K. Sugibayashi, Possibility and effectiveness of drug delivery to skin by needle-free injector, Int. J. Pharm. 391 (2010) 65–72.
[39] K. Benedek, E. Walker, L.A. Doshier, R. Stout, Studies on the use of needle-free injection device on proteins, J. Chromot. A 1079 (2005) 397–407.
[40] J. Seok, C.T. Oh, H.J. Kwon, T.R. Kwon, E.J. Choi, S.Y. Choi, S.K. Mun, S.-H. Han, B.J. Kim, M.N. Kim, Investigating skin penetration depth and shape following needle-free injection at different pressures: a cadaveric study, Lasers Surg. Med. 48 (2016) 624–628.
[41] J. Schramm-Baxter, S. Mitragotri, Needle-free jet injections: dependence of jet penetration and dispersion in the skin on jet power, J. Control. Rel. 97 (2004) 527–535.
[42] Y. Michinaka, S. Mitragotri, Delivery of polymeric particles into skin using needle-free liquid jet injectors, J. Controlled Rel. 153 (2011) 249–254.
[43] J. Baxter, S. Mitragotri, Jet-induced skin puncture and its impact on needle-free jet injections: experimental studies and a predictive model, J. Control. Release 106 (2005) 361–373.
[44] A. Taberner, N.C. Hogan, I.W. Hunter, Needle-free injection using real-time controlled linear Lorentz-force actuators, Med. Eng. Phys. 34 (2012) 1228–1235.
[45] L. Linn, B. Boyd, H. Ointchev, T. King, S.J. Farr, The effects of system parameters on *In Vivo* injection performance of a needle-free injector in human volunteers, Pharm. Res. 24 (2007) 1501–1507.
[46] S. Hama, M. Arata, I. Nakamura, T. Kasetani, S. Itakura, H. Tsuchiya, T. Yoshiki, K. Kogure, Prevention of tumor growth by needle-free injection of anti-C7orf24 siRNA, Cancer Gene Ther. 19 (2012) 553–557.
[47] G.E. Theintz, P.C. Sizonenko, Risks of jet injection of insulin in children, Eur. J. Pediatr. 150 (1991) 554–556.
[48] U. Schneider, R. Birnbacher, E. Schober, Painfulness of needle and jet injection in children with diabetes mellitus, Eur. J. Pediatr. 153 (1994) 409–410.
[49] A. Arora, I. Hakim, R. Rathnasingham, R. Srinivasan, D.A. Fletcher, S. Mitragotri, Needle-free delivery of macromolecules across the skin by nanoliter-volume pulsed microjets, PNAS 104 (2007) 4255–4260.
[50] Y. Tagawa, N. Oudalov, A. El Gahlbzouri, C. Sun, D. Lohse, Needle-free injection into skin and soft matter with highly focused microjets, Lab Chip 13 (2013) 1357–1363.
[51] V. Menezes, S. Kumar, K. Takayama, Shock wave driven liquid microjets for drug delivery, J. Appl. Phys. 106 (2009) 086102.
[52] J.E. Epstein, E.J. Gorak, Y. Charoenvit, et al., Safety tolerability, and lack of antibody responses after administration of a PfCSP DNA malaria vaccine via needle or needle-fre jet injection, and comparison of intramuscular and combination intramuscular/intradermal routes, Hum. Gene Ther. 13 (2002) 1551–1560.
[53] H. Okayasu, C. Sein, D.C. Blanc, et al., Intradermal administration of fractional doses of inactivated poliovirus vaccine: a dose-sparing option for polio immunization, J. Infect. Dis. 216 (2017) S161.
[54] D. Soonawala, P. Verdijk, A.J. Wijmenga-Monsurr, et al., Intradermal fractional booster of inactivated poliomyelitis vaccine with a jet injector in healthy adults, Vaccine 31 (2013) 3688–3694.
[55] M.T. Yousafzai, A.F. Saleem, O. Mach, A. Baig, R.W. Sutter, A.K.M. Zaidi, Feasibility of conducting intradermal vaccination campaign with inactivated poliovirus vaccine using Tropis intradermal needle free injection system, Karachi, Pakistan, Helyion 3 (2013) e00395.
[56] J. Ankersen, A.E. Birkbeck, R.D. Thomson, P. Vanezis, Puncture resistance and tensile strength of skin simulants, Proc. Inst. Mech. Eng, Part H: J. Eng. Med. 211 (6) (1999) 493–501.
[57] L.H. Jansen, P.B. Rottier, Some mechanical properties of human andominal skin measured on excised strips, Dermatologica 117 (1958) 65–83.
[58] L.H. Jansen, P.B. Rottier, Comparison of the mechanical properties of strips of human abdominal skin excised from below and from above the Umbilic, Dermatologica 117 (1958) 252–258.
[59] M.S. Schneider, J.E. Borkow, I.T. Cruz, R.D. Marangoni, J. Shaffer, D. Grove, The tensiometric properties of expanded Guinea pig skin *Plastic & Recon*, Surg. 81 (3) (1988) 398–403.
[60] M. Thomsen, A. Hernandez-Garcia, J. Mathiesen, M. Poulsen, D.N. Sorensen, L. Tarnow, R. Feidenhans, Model study of the pressure build-up during subcutaneous injection, PLoS One 9 (2014) e104054.
[61] G. Park, A. Modak, N.C. Hogan, I.W. Hunter, The effect of jet shape on jet injection, IEEE Conf. Proc. 2015, pp. 7350–7353.